Combustion and Flame 256 (2023) 112915

Contents lists available at ScienceDirect

Combustion and Flame

journal homepage: www.elsevier.com/locate/combustflame

Air-blast atomization and ignition of a kerosene spray in hot vitiated crossflow

Luigi Miniero[a,*], Khushboo Pandey[a], Daniel Fredrich[b], Sergey Shcherbanev[a], Ulrich Doll[c], Andrea Giusti[b], Nicolas Noiray[a,*]

[a] CAPS Laboratory, Department of Mechanical and Process Engineering, ETH Zürich, Zürich 8092, Switzerland
[b] Department of Mechanical Engineering, Imperial College London, Exhibition Rd, London SW7 2AZ, UK
[c] Experimental Thermal Hydraulics Group, Paul Scherrer Institute, Forschungstrasse 111, Villigen PSI, 5232, Switzerland

ARTICLE INFO

Article history:
Received 15 February 2023
Revised 11 June 2023
Accepted 20 June 2023

Keywords:
Spray in vitiated crossflow
Kerosene
Air-blast atomization

ABSTRACT

Increasingly stringent regulations of pollutant emissions from aviation require rapid implementation of novel combustion technologies. Promising concepts based on moderate or intense low-oxygen dilution (MILD) combustion have been investigated in academia and industry. This MILD regime can be obtained from the recirculation of the hot vitiated combustion products to raise the temperature of the reactants, resulting in distributed reaction regions and lower flame temperatures. In the present work, we consider the air-blast atomization of a kerosene spray in crossflow, which enables efficient mixing between fuel and oxidizer. We investigate experimentally and numerically the effect of the spray air-to-liquid mass-flow ratio (ALR) variation on the reaction front and flame topology of a kerosene spray flame. The spray is injected transversely into a turbulent vitiated crossflow composed of the products of a lean CH_4-H_2 flame. The spray flame thermal power is varied between 2.5 and 5 kW, along with the atomizer ALR between 2 and 6. The experimental characterization of the reaction zone is performed using OH^* chemiluminescence and OH and fuel planar laser-induced fluorescence (PLIF). The Large Eddy Simulations (LES) of the multiphase reactive flow provide good agreement with the experimental observations. Experiments and simulations show that the ALR governs mixing, resulting in different flame stabilization mechanisms and combustion regimes. Low ALR results in a relatively small jet-to-crossflow momentum ratio and a large spray Sauter mean diameter (SMD). A thick windward reaction region is formed due to inefficient shear layer mixing between the fuel spray and the crossflow. Meanwhile, the correspondingly large spray SMD leads to isolated penetration and localized combustion of fuel clusters. At high ALR, the higher penetration and the faster droplet evaporation due to the lower spray SMD result in an efficient entrainment-induced mixing between the two streams, forming more distributed reaction regions.

1. Introduction

The steady growth of air traffic in recent years has raised regulatory attention aiming at curbing the impact of aviation on climate change by 2050 [1]. This objective demands the rapid development of novel aeroengines combustion technologies capable of reducing CO_2 and non-CO_2 emissions while ensuring safe flight operation [2]. In this context, one of the most attractive combustion concepts is the 'Moderate or Intense Low-oxygen Dilution' (MILD) [3], as it has shown promising results of low NO_x, CO, soot, and noise emissions for gaseous fuel operations [4,5], and in-furnace applications [6,7]. The MILD combustion regime is based on preheating reactants above their autoignition temperature through efficient mixing with products [8], resulting in a relatively low-temperature increase during the combustion process [9]. Burners operated under this regime have shown emissions reduction and possible applicability to gas turbines. Galletti et al. [10] operated an industrial furnace under MILD combustion conditions through internal recirculation of exhaust gases. They modeled it numerically and validated the simulations against experimental measurements of species concentrations and temperature. A significant reduction of NO emissions and a more uniform temperature distribution on the outer surfaces of the burner were reported for MILD conditions compared to the standard operation. Sorrentino et al.

* Corresponding authors.
E-mail addresses: minierol@ethz.ch (L. Miniero), noirayn@ethz.ch (N. Noiray).

https://doi.org/10.1016/j.combustflame.2023.112915

[11] observed the onset of the MILD regime in the cyclonic burner, designed to achieve efficient turbulent mixing between reactants and a long residence time for combustion. They varied preheating temperature and the diluent composition between N_2 and CO_2, reporting low flame luminosity and uniform temperature distribution in the chamber in MILD operation. Szegö et al. [12] investigated a parallel jet MILD furnace, reporting weak dependency of NO formation on the overall low temperature in the burner. They concluded that the formation of NO through the thermal pathway is substantially reduced for MILD combustion, comparable to prompt-NO and/or N_2O-intermediate ones. Iavarone et al. [13] have compared different models to predict computationally NO_x formation to the exhaust of a gaseous MILD burner. The reported low NO emissions are modelled with chemical pathways normally negligible compared to thermal NO in conventional combustion systems. The low combustion temperature and dilution at MILD conditions increases the residence time necessary for thermal NO formation [14]. El Helou et al. [15] investigated the behavior of a non-premixed methane-air Lean Azimuthal Flame (LEAF) burner. The burner's concept is based on a jet in hot crossflow configuration, where air from the top of the burner entrains fuel and combustion products into a vitiated toroidal flow. The strong recirculation of high-temperature products increases the temperature of the reactants that subsequently burn in the MILD combustion regime, leading to low NO, UHC, and CO emissions. The burner operation was later extended to kerosene injected from pressure-swirl atomizers by de Oliveira et al. [16]. Miniero et al. [17] investigated a new dual-fuel version of the LEAF burner presented in Oliveira et al. [16], featuring several geometrical modifications and an air-assisted mode of atomization, operated with hydrogen and kerosene. They related the topology of the LEAF reaction region and the soot formation in the combustion chamber to the dual effect of the atomizer air-to-liquid mass-flow ratio (ALR) on the spray-to-crossflow momentum ratio and the spray Sauter Mean Diameter (SMD). A constant mass flow of hydrogen was injected into the burner to extend the operating range of the toroidal LEAF flame towards lower ALR conditions. In a separate work, Pandey et al. [18] studied the topological transition of the LEAF toroidal flame to a tubular flame at low ALRs without hydrogen injection. The phenomenon was explained using a basic phenomenological model incorporating spray evaporation and the convective flow timescales of each operating condition.

The promising results of emissions reduction in gaseous MILD burners, combined with the growing availability and technological maturity of liquid sustainable aviation fuels (SAF) [19], have increased the research interest in MILD combustion of liquid fuels. However, there are still many fundamental questions regarding spray combustion in vitiated environments [20]. The complexities associated with multiphase reacting flows require an in-depth understanding of the evaporation rate, ignition dynamics, and flame stabilization mechanism [21]. Recent studies have focused on different academic configurations to achieve efficient mixing, such as sprays in co-flows, and crossflows, to analyze these phenomena.

Williams et al. [22] analyzed the characteristics of the autoignition kernels of a Jet A spray in a vitiated co-flow as a function of its temperature. They observed that for lower co-flow temperatures, the autoignition is initiated randomly in small kernels that increase their dimension and equivalence ratio while being convected downstream. On the contrary, when the co-flow temperature is increased, the autoignition happens in larger rich kernels, which do not vary their equivalence ratio as they move downstream. Rodrigues et al. [23] observed changes in the local flame type and the heat release rate in a pressure-swirl ethanol spray flame by varying the co-flow from ambient to hot-diluted air. The effect of a lower oxygen concentration and the higher temperature was reflected in an increase in the evaporation rate and larger entrainment of the co-flow, leading to a reduction of the peak temperatures in the flame region. The same test case was later numerically investigated by Ma and Roekaerts [24] and Gallot-Lavallée et al. [25]. The former found a transition in the flame structure from a 'double flame' to a 'single flame' when changing the co-flow conditions from ambient to hot-diluted air. The latter showed that the droplet size distribution is a key parameter affecting the flame stabilization mechanism.

The jet in crossflow has been extensively studied due to its applicability to many engineering fields [26]. The complex vortical structure of this configuration has been proven to provide a better mixing between the two streams when compared to free jets [27]. In particular, the application of a reactive gaseous jet in vitiated crossflow to gas turbines with sequential combustion [28] has sparked research interest both for premixed [29–31] and non-premixed jets [32–34]. In the case of the premixed air ethylene jet in hot vitiated crossflow experimentally investigated in Wagner et al. [30], it was demonstrated in the numerical investigation presented in Schulz et al. [35] that an autoignition cascade develops along the windward side of the jet: the heat release peak occurs for very lean mixtures at the root of the jet, and it drifts towards stoichiometric mixture along the windward shear layer due to heat diffusion. The self-ignition process of this configuration was also unraveled and investigated in Solana-Pérez et al. [36]. In [34], the behavior of a transverse methane jet in a vitiated turbulent crossflow burning in MILD conditions was investigated. The oxygen concentration in the crossflow affected the shape of the reaction region without significantly contributing to the intensity of the OH^* chemiluminescence signal. Moreover, the MILD region was formed of thin flame fronts for all the investigated operating conditions. The injection of partially atomized fuel into a crossflow has not received significant attention, despite its advantages in terms of mixing length reduction compared to liquid jets, which is beneficial for the onset of MILD combustion. Two well-established efficient methods to achieve fuel atomizations are pressure-swirl and air-blast atomizers. The latter has several advantages over the former atomization mode for gas turbine applications. It requires lower fuel-delivery pressures and provides premixing of the liquid fuel with a small amount of air before mixing with the main oxidizer stream [37]. Furthermore, the flexibility in terms of spray penetration, droplet size, and dispersion of air-blast atomizers enables optimization of their performance at different operating conditions. Leong et al. [38] extensively studied a Jet A-1 air-blast spray injected into a crossflow of air at ambient conditions. They observed an increase in the spray penetration and degree of atomization by increasing the air-blast pressure drop. Sinha et al. [39] reported that the spray trajectory of an air-blast atomizer in an air crossflow at ambient conditions depends primarily on the ALR of the atomizer and the liquid surface tension. While the first parameter holds information on the air-blast velocity, the second affects the droplets' drag force in the crossflow. Therefore, this configuration has to be described by accounting for the characteristics of both the gaseous atomization air jet and the droplet behavior in a turbulent crossflow.

The application of MILD combustion to liquid fuels for aero-engine applications calls for fundamental studies of reactive sprays in vitiated crossflow. Unlike gaseous jets with long-standing literature, studies focused on reactive liquid sprays in the vitiated environments remain scarce to date, despite their potential for low-emissions combustion concepts. In such a configuration, the multi-phase physics of liquid spray combined with spatio-temporal scales of reacting fields presents inherently and intrinsically complex problems [17,40].

The present study aims at characterizing the flame topology, mixing characteristics, and reaction fronts, of a kerosene spray in a hot vitiated crossflow as a function of the air-to-liquid ratio of an

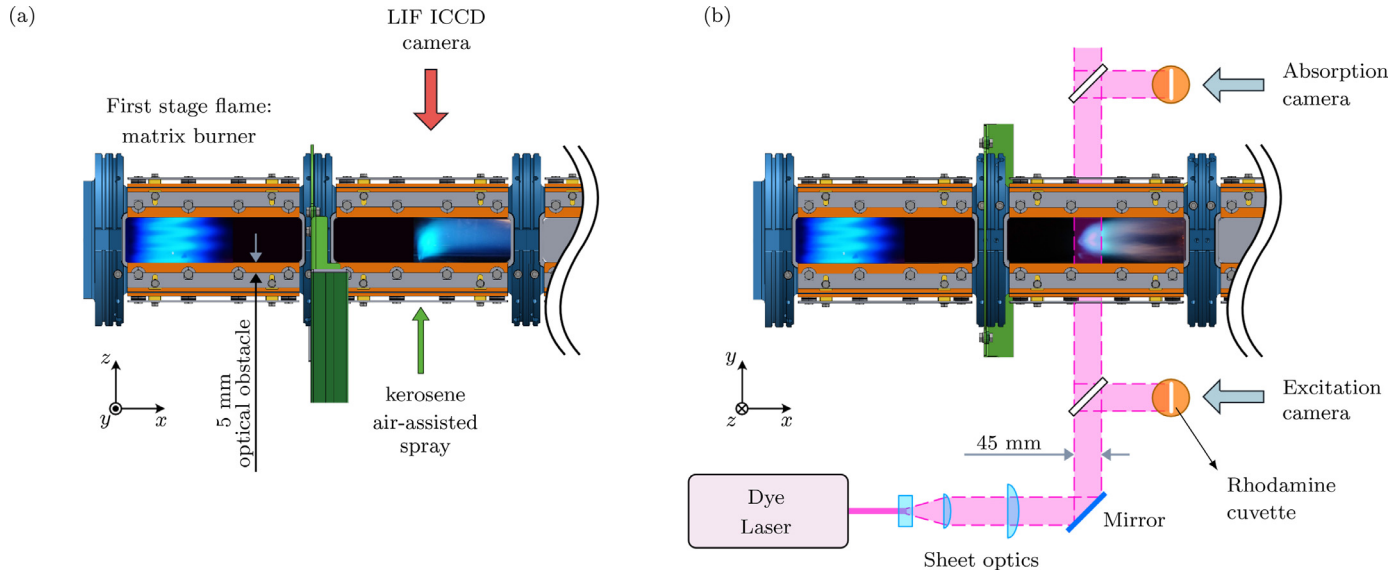

Fig. 1. Sketches of the test rig depicting (a) the side-view ($x-z$ plane) of the first-stage flame and the spray flame, and (b) the top-view ($x-y$ plane) of the first-stage flame and the spray flame along with the location of the laser sheet employed for the PLIF measurements.

air-blast atomizer. The fundamental analysis of this configuration provides a stepping stone for understanding spray combustion in the vitiated environment. Insights into the complexity of the multiphase turbulent reactive flow physics are obtained at different positions along the jet trajectory employing both experiments and Large Eddy Simulations (LES). The experiments include OH* chemiluminescence and OH planar laser-induced fluorescence (PLIF) on different planes. The experimental results are complemented with time-resolved, three-dimensional numerical data to provide additional insights into the velocity field and spray characteristics. This data is acquired by applying an in-house LES code with Eulerian-Lagrangian formulation and a transported probability density function combustion model, extending the work previously carried out by Fredrich et al. [40].

The paper is organized as follows. Section 2 describes the experimental set-up, and Section 3 introduces the numerical method employed in the study. The experiments are presented in Section 4, and complemented in Section 5 with the analysis of the Large Eddy Simulations results. Final remarks conclude the paper.

2. Experimental set-up

2.1. Test rig

The experiments are conducted using a generic modular staged combustor with a square cross-section of 62 × 62 mm^2, operated at atmospheric pressure. A 4 × 4 array of lean turbulent CH_4-H_2-Air technically-premixed flames composes the first stage. The equivalence ratio and thermal power of the first stage are kept constant at 0.7 and 50 kW, respectively, with a 5% H_2 enrichment in mass. A Jet A-1 kerosene spray is injected 348 mm downstream of the first stage flame through an internal-mixing air-blast atomizer (Delavan: SN type-30610-1) which is encased in an aluminum jacket and water-cooled to 353 K (temperature measured with a *K*-type thermocouple). Kerosene is injected through a liquid orifice with a diameter of $d_{liq} = 0.6$ mm and atomised by shear by an air stream coming from a torus concentric to the liquid orifice and with inner and outer diameter of $d_{in} = 1.1$ mm and $d_{out} = 1.8$ mm. Further details on the atomiser and its geometry are included in Fig. 1 of [41]. The operating conditions and the corresponding values of the global equivalence ratio ϕ, jet-to-crossflow momentum ratio (J), and spray Sauter Mean Diameter (SMD) are summarised in Table 1. The average density and species composition of the crossflow is calculated with a CANTERA 0D equilibrium calculation of the first stage flame [42]. It is important to underline that the variation of the atomizer ALR does not substantially affect the global equivalence ratio of the flow ϕ at constant thermal power, which remains lean for all the operating conditions ($\sim 4.5\%$ of ϕ). The jet-to-crossflow momentum ratio J for an air-blast atomizer is calculated by the relation introduced using Leong et al. [38]:

Table 1
Operating conditions.

OC #	P_k [kW]	ALR [−]	ϕ [−]	J [−]	SMD [μm]
1	2.5	2	0.12	18	53.9
2	2.5	6	0.12	162	20.8
3	5	2	0.22	61	33.8
4	5	6	0.21	547	13.5

$$J = \frac{(\rho_k U_k^2 A_k + \rho_{ab} U_{ab}^2 A_{ab})/A_s}{\rho_{cf} U_{cf}^2}, \tag{1}$$

where ρ, U and A indicate the density, velocity, and cross-sectional area of the atomizer relative to kerosene (k), air-blast air (ab), and vitiated crossflow (cf), respectively. The area A_s is the sum of A_k and A_{ab}. The previous experimental results of Chong et al. [41] and Kumar et al. [43] show that the spray Sauter Mean Diameter (SMD) of the atomizer used in the present work closely follows the empirical correlation presented by Rizk and Lefevbre [44] for a plain jet air-blast atomizer. The spray SMDs are calculated using this correlation for all operating conditions for the presented work.

2.2. Experimental diagnostics

The high-speed OH* chemiluminescence imaging of the spray flame is done using a LaVision Highspeed camera coupled with an IRO intensifier oriented along the *y*-direction of Fig. 1. A UV lens (Cerco 100 mm f2.8) together with a bandpass filter (Chroma, $T > 70\%$ at 310 nm, FWHM 10 nm) is mounted to the intensifier. The OH* flame images are acquired at 5 kHz and up to 1000 images (0.2 s of acquisition time). The IRO gain and gate are kept constant for all the operating conditions. The experimental setup

for the OH PLIF imaging consists of a frequency-doubled dye laser (Quantel TDL 90 pumped with YG981, 20 mJ per pulse, 0.08 cm-1 FWHM) tuned to the Q1(8) transition of the OH(A-X) ($\nu' = 1$, $\nu'' = 0$) band near 283.55 nm. The laser beam is expanded into a 44 mm wide sheet using a combination of cylindrical lenses and aligned in the $x-y$ plane (see Fig. 1(b)). The excited OH-fluorescence signals are captured with an ICCD camera (PCO Dicam Pro), oriented along the z axis (depicted in Fig. 1(a)). The camera is equipped with a UV lens (Cerco 100 mm f2.8) together with a bandpass filter (Chroma, $T > 70\%$ at 310 nm, FWHM 10 nm). 200 OH PLIF images (20 s acquisition time) are recorded at a sampling rate of 10 Hz with a spatial resolution of 136 μm/pixel. The laser sheet profiles are measured by sampling part of the laser light onto cuvettes filled with rhodamine 6G dye solution before (excitation profile) and after (absorption profile) the test section. These profiles are recorded with two CCD cameras (PCO Pixelfly with Schneider–Kreuznach 25 mm f/1.95 lens). The above-mentioned optical elements and the imaging setup are mounted on an electric traverse system (Isel Gantry Flatbed Cartesian Robot) to move the configuration along the z-direction in 5 mm steps.

Additionally, to provide a mid-section across the entire span of the jet in crossflow, the lateral quartz window was replaced with the water-cooled aluminum plate housing the atomizer, and the OH PLIF light sheet was aligned with the injector tip. In this configuration, the laser sheet is blocked by the anodized plate, and the absorption profile cannot be measured, which precludes OH concentration measurement and only allow qualitative OH PLIF imaging in this configuration.

Note that the window frame (see the orange area, Fig. 1(a)) constitutes an optical obstacle of 5 mm from the chamber wall so that, e.g., the point of injection is not visible.

2.3. Kerosene fluorescence and OH concentration/temperature measurements

The PLIF instrumentation is used for two purposes: (1) to identify the fuel spray in the unburnt region of the jet in vitiated crossflow and (2) to determine the absolute OH concentration, converted into temperature fields in the burnt zones when certain criteria are met. To achieve the first, the laser wavelength detuned from the absorption line (off-resonance-case). The acquired camera intensities then represent the remainder of flame chemiluminescence in the burnt and the kerosene fluorescence in the unburnt flow region, which is mainly related to the kerosene's aromatic content when excited at 283 nm [45]. To accomplish the second, the laser wavelength is tuned back to the absorption line (on-resonance-case) and the simultaneous measurement of OH PLIF and OH laser absorption is used to determine the local OH concentration from a single laser pulse [46,47]. The mean intensity of the off-resonance images is subtracted from the on-resonance cases to scale them to the OH LIF intensity. Furthermore, both the conditions are scaled with the ratio between the incoming (excitation) and the outgoing (absorption) laser profiles, and corrected for the flame chemiluminescence and camera background. The local LIF intensity generated by the laser sheet tuned the OH absorption line is related to the absolute OH concentration in two steps. First, the LIF signal is scaled with the local laser intensity and the local spectral overlap between the laser and the absorption line. In the second step, local absorption is approximated as a function of the local normalised LIF intensity, as each absorbed photon will result in a LIF signal with a probability described by the fluorescence quantum yield. Finally, the measured absorption is expressed as a measure of number density, i.e., the OH concentration [48]. The method can be extended to temperature measurements when the OH density is nearly independent of ϕ, i.e., under the assumptions of chemical equilibrium and a globally lean mixture ($\phi < 0.9$). In this case, the OH concentration can be considered dependent on temperature only. Therefore, CANTERA [42] equilibrium calculations of the reactants at different temperatures are employed to relate the measured OH concentrations to temperature values. The technique has a lower temperature detection limit of 1300 K and an uncertainty below 5% in the 1600–2100 K range [47]. It has been recently applied to a similar setup by Weilenmann et al. [49], and at higher pressure conditions by Doll et al. [50]. The above-mentioned assumptions are applicable downstream of the first-stage flame without the spray injection for the presented experiments. Hence, the crossflow temperature field without the spray is obtained at different z positions from the OH density maps.

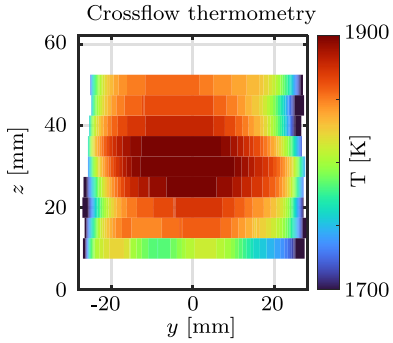

Fig. 2. Reconstructed temperature distribution of the combustor cross section ($y-z$ plane) obtained by means of planar OH thermometry, where [0;0] corresponds to the atomizer location.

Figure 2 presents the average temperature field for the combustor cross section ($y-z$ plane in Fig. 1). It is obtained by averaging the temperature distribution on $x-y$ planes along the x axis at different z heights and reconstructing the temperature field for the $y-z$ plane. The average temperature is used as one of the boundary conditions for the LES set-up.

As discussed above, the module employed for the spray injection is composed of three air-cooled quartz windows and a water-cooled bottom plate mounted with the spray atomizer and maintained at 353 K. The difference in the boundaries is reflected in a lower temperature close to the bottom wall.

3. Numerical method

All simulations are performed with the LES code BOFFIN [51]. The code is based on a second-order accurate finite volume method and uses a pressure-based, low-Mach number, variable density formulation. Sub-grid scale turbulence-chemistry interactions are closed via a transported probability density function approach solved by the Eulerian stochastic fields method. A comprehensive reaction mechanism with 57 species (based on Ref. [52]) is applied, where dodecane is used as a single-component fuel surrogate to represent kerosene (Jet A-1)-air combustion. An Eulerian-Lagrangian framework accounts for the two-way coupling between the continuous and dispersed phases of the flow. The droplet evaporation rates are computed with the rapid mixing model [53], while secondary breakup is neglected (dilute spray regime). A stochastic dispersion model is included following the work of Bini and Jones [54], and drag is assumed to be the only force acting on the droplets.

The square duct domain is discretized by a mesh consisting of approximately 8×10^6 cells [40] extending 70 mm upstream and 180 mm downstream of the fuel atomizer. A vertical temperature profile based on the experimental thermometry results is prescribed at the crossflow inlet, along with a fully-developed turbulent velocity profile. The vitiated flow conditions in the crossflow are taken from the aforementioned equilibrium calculation of the

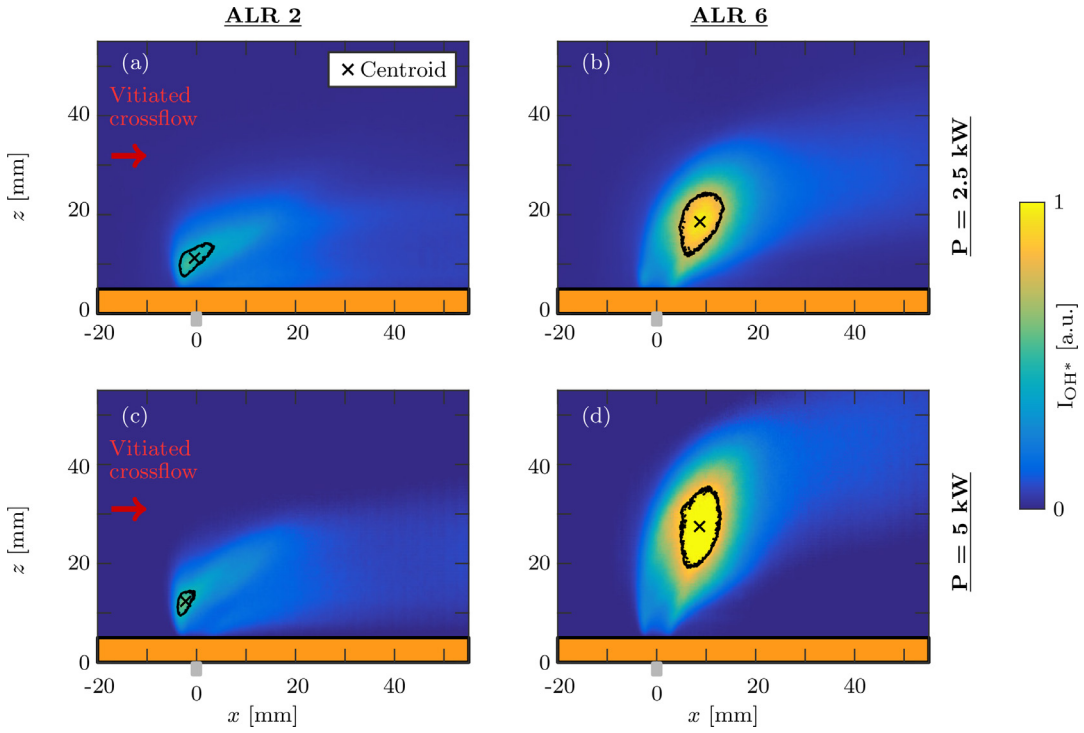

Fig. 3. The normalized time-averaged OH* chemiluminescence at (a) OC1, (b) OC2, (c) OC3, and (d) OC4. The intensities are normalized by the maximum values among all the operating conditions. The black iso-contour highlights the 25% boundary of the maximum intensity for each case. The x symbols indicate the position of the centroid of the area delimited by the isocontour.

first-stage flame. The wall heat transfer is treated through the application of isothermal wall temperatures as per the experimental measurements. The fuel spray is injected from a point source using a Rosin-Rammler droplet size distribution based on the estimated SMD for each ALR (see Table 1) and a dispersion parameter equal to 4. The inflow velocities of the fuel droplets and the surrounding kerosene jet are computed from the respective mass flow rates and injection diameters using an inlet temperature of 300 K for both streams. More details on the computational setup can also be found in Fredrich et al. [40].

4. Experimental results

4.1. Global spray flame characteristics

The OH* chemiluminescence signature is widely regarded as the heat release marker for laminar and lean premixed flames [55]. However, several studies have highlighted the inadequacy of OH* signals to accurately estimate the heat release rate of turbulent flames, where the chemiluminescence intensities are substantially affected by turbulent flow structures, and local variations of the equivalence ratios [56,57]. Additionally, the line-of-sight intensity integration of the chemiluminescence images limits the spatial resolution to global flame heat release regions without detailing the small-scale intricacies [58]. In the current work, the kerosene spray combustion in a turbulent vitiated environment attributes to a highly three-dimensional and non-premixed phenomenon. Hence, the spray flame OH* chemiluminescence images are solely utilized to present and describe the global flame shape features [59].

Figure 3 reports the normalized and time-averaged OH* chemiluminescence results for the four operating conditions of Table 1. First, the remnants of first stage OH* intensities are removed from the acquired spray flame images through background subtraction. Afterward, these images are used to evaluate average OH* intensity fields and are normalized by the maximum intensity value among the operating conditions. The black iso-contour highlights the 25% boundary of the maximum intensity for each case, drawn to identify the location of highly reacting regions. The position of the centroid of this area provides an indication for the analysis of the reaction characteristics accounting for the variation of the flame penetration at different ALRs in the remainder of the paper. A similar approach has been employed in premixed and non-premixed hydrogen jets in crossflow in Solana-Pérez et al. [29] to study the jet flame morphology and penetration and to identify the flame shape and center of gravity in the second stage of a RQL setup in Renner et al. [60].

Interestingly, the global flame characteristics of the two kerosene thermal power conditions exhibit similar observations with the ALR variations, including the relocation of intense reaction regions, as depicted by the black iso-contours in Fig. 3.

The high-intensity flame regions are located predominantly upstream of the spray flame and close to the injection point for ALR 2 (Fig. 3(a) and (c)). However, by increasing the ALR to 6 (b and d), these intense regions are moved further downstream. The higher spray penetration results in a lifted flame from the injection point such that the centroid of the high-intensity region is shifted from $z \sim 15$ mm to ~ 25 mm above the injection.

In the following, OH and fuel PLIF measurements are performed to further comment on the spray flame features and the associated controlling parameters. The corresponding results are described in the next sections, focusing on the higher power cases (OC3 and OC4).

4.2. Flame topology and fuel distribution

Figure 4 reports the average OH PLIF and the maximum fuel PLIF intensity of each pixel on the central ($y = 0$) $x - z$ plane at ALR 2 and 6. At ALR 2 (Fig. 4(a)), a high OH LIF signal is observed on the windward side of a strongly bent non-reacting jet with lower jet penetration than for ALR 6. Furthermore, the fuel PLIF (Fig. 4(b))

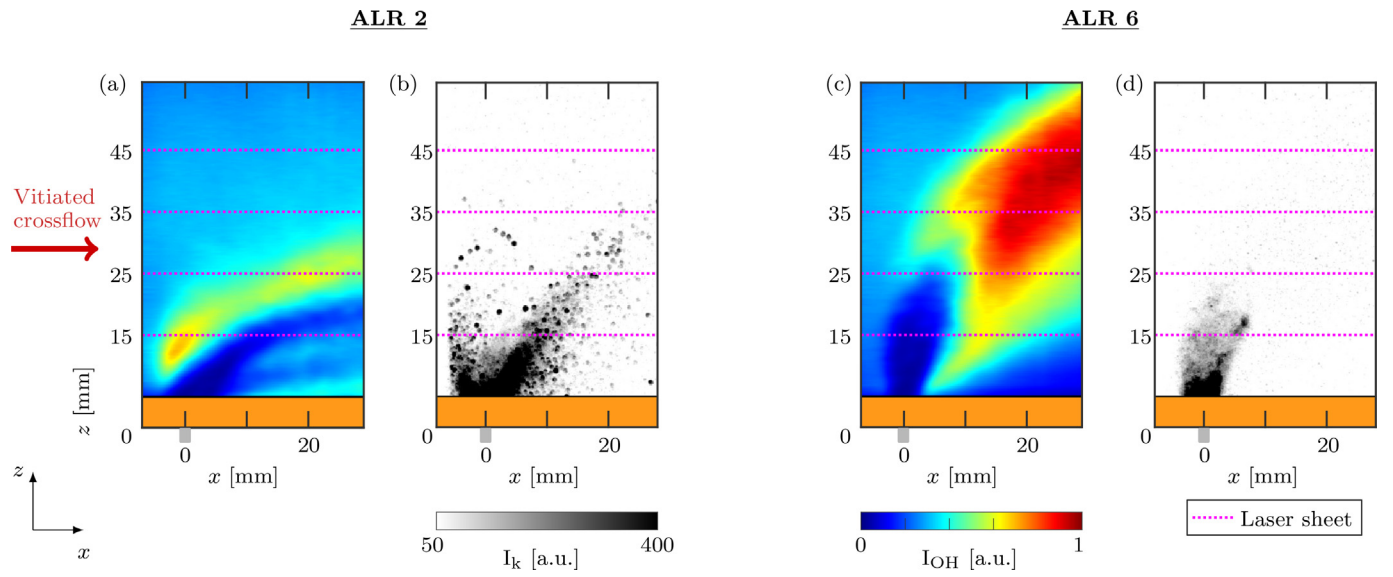

Fig. 4. (a) time-averaged OH PLIF signal on the central ($y = 0$ mm) $x - z$ plane normalized by the maximum intensity of each pixel for OC3 (thermal power 5 kW ALR 2), (b) maximum kerosene PLIF intensity of each pixel for OC3 (thermal power 5 kW ALR 2), (c) time-averaged OH PLIF signal on the central ($y = 0$ mm) $x - z$ plane normalized by the maximum pixel of each pixel for OC4 (thermal power 5 kW ALR 6), and (d) maximum kerosene PLIF intensity of each pixel for OC4 (thermal power 5 kW ALR 6). The horizontal dotted lines represent the position of the laser sheet for the PLIF measurements on the $x - y$ planes at different z locations.

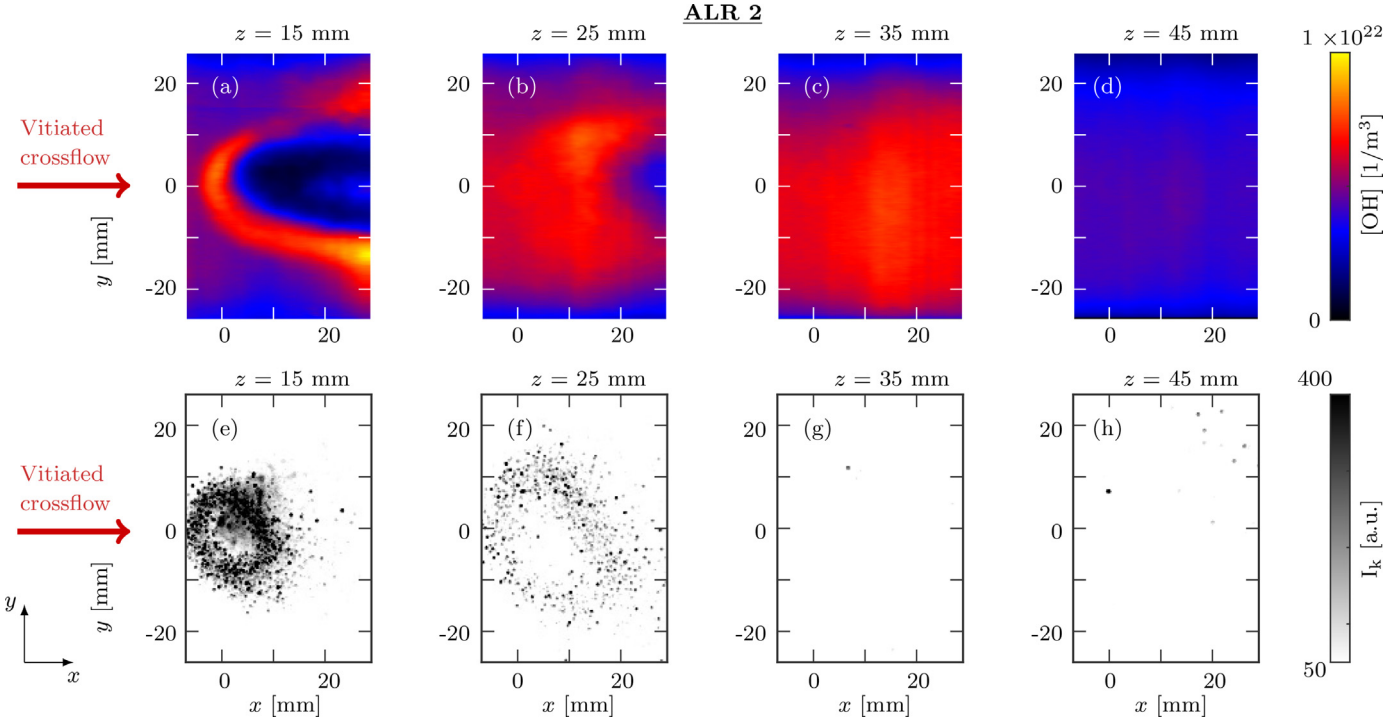

Fig. 5. Experimental time-averaged OH density fields at OC3 (5 kW of thermal power and ALR 2) on the $x - y$ planes at (a) $z = 15$ mm, (b) $z = 25$ mm, (c) $z = 35$ mm, and (d) $z = 45$ mm, above the spray injection location. Maximum kerosene PLIF intensity of each pixel for OC3 (5 kW of thermal power and ALR 2) on the $x - y$ planes at (e) $z = 15$ mm, (f) $z = 25$ mm, (g) $z = 35$ mm, and (h) $z = 45$ mm.

shows a sporadic distribution of kerosene clusters. The OH PLIF signal at ALR 6 (Fig. 4(c)) confirms the relocation of the high OH intensity area to the leeward side, as previously observed from the OH* chemiluminescence images. In this case, fuel PLIF intensities are primarily concentrated in the vicinity of the spray injection point, as shown in Fig. 4(d).

Figures 5 and 6 show average OH planar density distributions (a–d) in the $x - y$ plane and the maximum intensity of each pixel over the whole set of acquired images of the fuel PLIF (e–h) at different z locations for OC3 and OC4. At ALR 2, at $z = 15$ mm (Fig. 5(a)), high OH density regions enclose the non-reacting jet (areas with minimal OH densities). The formation of these regions can be attributed to the shear-dominated mixing process between the fuel and the vitiated crossflow [61]. The plane $z = 25$ mm (b) exhibits a similar distribution of OH density, with an extended windward region of high OH concentration. Additionally, due to the small jet penetration in the crossflow, the regions pertaining to the non-reacting jet do not extend beyond $z \geq 35$ mm (Fig. 5(c)). Instead, a well-distributed area of high OH densities is observed that corresponds to the products of the windward reaction zone on the

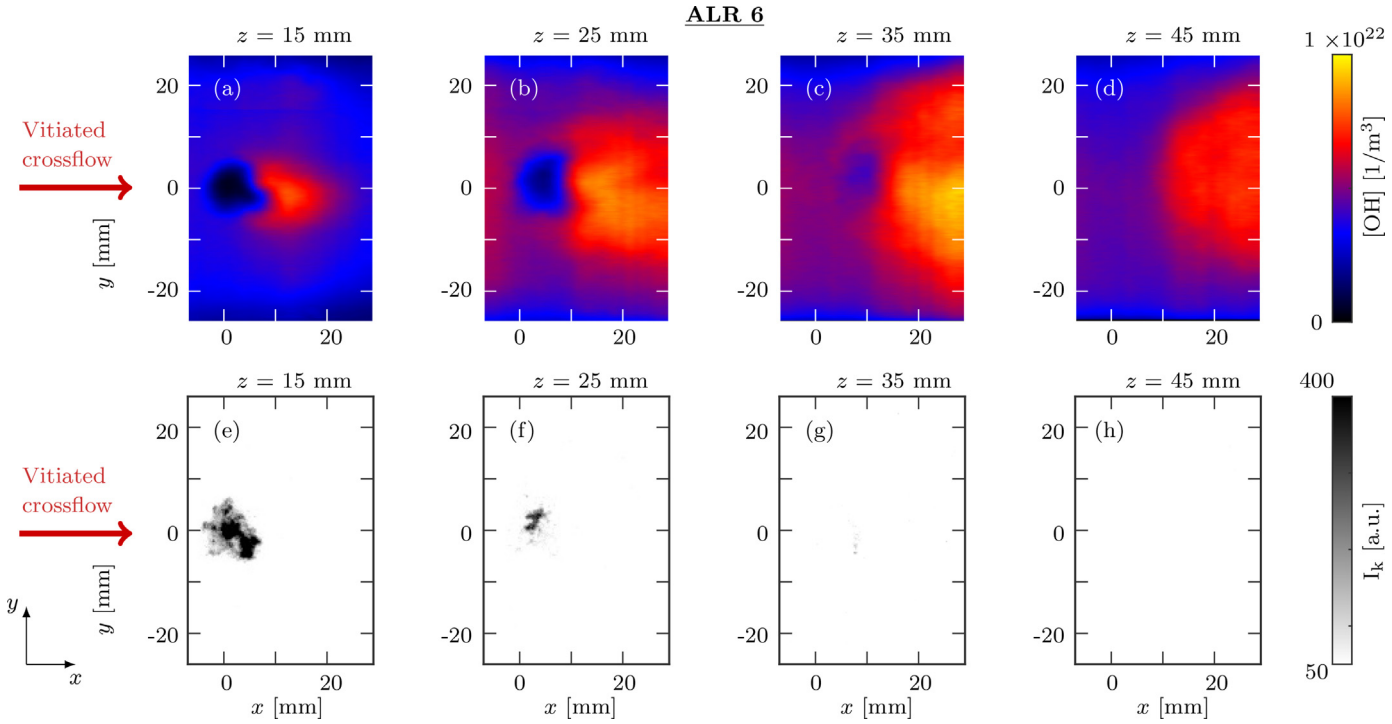

Fig. 6. Experimental time-averaged OH density fields at OC4 (5 kW of thermal power and ALR 6) on the $x-y$ planes at (a) $z = 15$ mm, (b) $z = 25$ mm, (c) $z = 35$ mm, and (d) $z = 45$ mm, above the spray injection location. Maximum kerosene PLIF intensity of each pixel for OC4 (5 kW of thermal power and ALR 6) on the $x-y$ planes at (e) $z = 15$ mm, (f) $z = 25$ mm, (g) $z = 35$ mm, and (h) $z = 45$ mm.

lower planes. On average, no significant OH density areas are detected at $z = 45$ mm (Fig. 5(d)).

Large fuel PLIF $x-y$ signals are measured close to the injection position ($z \leq 25$, Fig. 5(e) and (f)), in the form of localized clusters distributed around a circular shape. The low penetration of the air-assisted spray in the crossflow due to smaller J inhibits crossflow entrainment, resulting in a weak mixing on the leeward side. At the same time, bigger droplets tend to penetrate the crossflow without following the atomization air due to their large inertia. At higher $x-y$ planes, no significant fuel clusters are detected.

At ALR 6, regions of high OH concentration are stabilized downstream of the stiff kerosene jet for $z < 45$ mm (Fig. 6(a)–(c)). They gradually increase their area due to the contribution of mixing and reaction at lower planes. The high-velocity jet penetrates the crossflow, increasing the entrainment-induced mixing between the two streams on the leeward side. As a result, a transition from the non-reacting jet to the high OH density area is observed along the jet trajectory (at $z = 45$ mm Fig. 6(d)). The fuel PLIF signals are relatively uniform and locally confined to regions where lower OH densities are observed (Fig. 6(e) and (f)). At $z = 35$ and 45 mm, no significant fuel clusters are detected. This further suggests that at ALR 6, entrainment-induced mixing and subsequent formation of the combustible mixture occur in the non-reacting regions.

4.3. Reaction fronts with ALR variations

Figure 7 reports the instantaneous OH density in the $x-y$ planes at multiple z locations for OC3 (a–d) and OC4 (e–h).

Close to the injection point ($z \leq 25$, Fig. 7(a) and (b)), the windward high OH density region is formed by a thick layer enclosing the non-reactive jet. In this area, the jet mixes with the vitiated crossflow, and it reacts. At higher planes, localized high OH density clusters are identified in the reaction region ($z > 15$ mm, Fig. 7(b)–(d)). These correspond to individual reacting fuel clusters generated by droplets that do not follow the atomization air jet and penetrate individually in the crossflow.

At ALR 6, substantial changes compared to ALR 2 in the shape of the instantaneous OH maps are observed (Fig. 7(e-h)). The sharp localized gradient of OH concentration on the leeward side of the jet highlights that the reaction region is now locally predominantly formed by distinct corrugated thin flame fronts at all the planes. As discussed before, the high ALR case features a strong mixing between fuel and the hot vitiated oxidizer, enhanced by the rapid evaporation of the droplets. The observation of thin flame fronts was related in literature to the onset of MILD combustion regime in gaseous conditions both experimentally [34] and numerically [62]. The present work reports results that point towards a similar trend for liquid fuel combustion in the MILD regime.

5. Numerical results

In the following sections, the LES results provide further insights on the intricate dependence of the reaction zone formation and fuel distribution on the mixing and spray characteristics.

5.1. Mixing mechanism

Figure 8 shows instantaneous snapshots of OH and dodecane mass fractions on the $x-z$ plane at $y = 0$ for the LES of OC3 and OC4. The black iso-contours represent 10% of the maximum heat release rate (HRR) for the respective operating conditions.

Figure 8 confirms the relocation of the regions with high OH mass fractions from the windward to the leeward side with ALR variation from ALR 2 (Fig. 8(a)) to ALR 6 (c). These results are in good agreement with experimental observations of the previous sections, as shown in Fig. 4. At ALR 2, reaction fronts are concentrated on the windward side of the jet, superposed to the high OH density area, as highlighted by the heat release rate isocontour in Fig. 8(a). A significant OH concentration is detected on the far field,

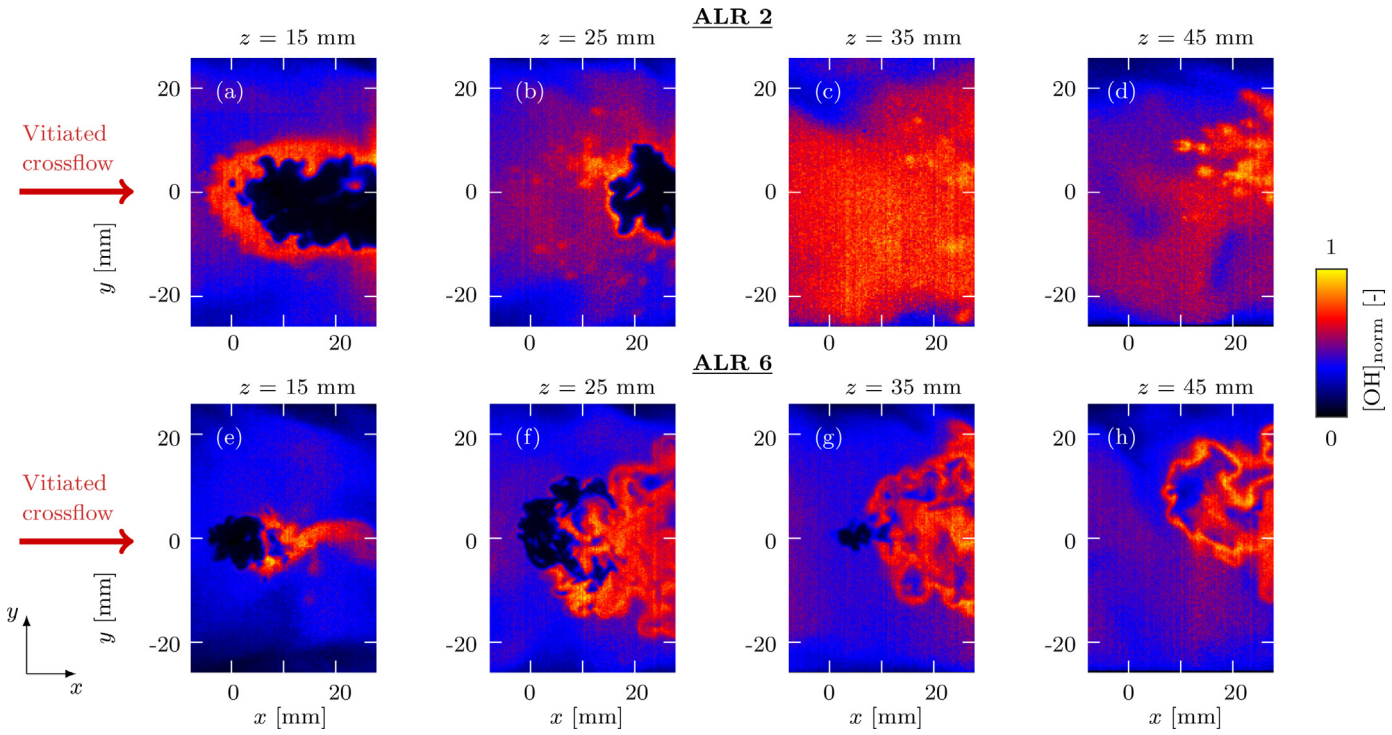

Fig. 7. Experimental normalized instantaneous $x-y$ OH density fields for OC3 (5 kW of thermal power and ALR 2) at (a) $z = 15$ mm, (b) $z = 25$ mm, (c) $z = 35$ mm, and (d) $z = 45$ mm. Experimental normalized instantaneous $x-y$ OH density fields for OC4 (5 kW of thermal power and ALR 6) at (e) $z = 15$ mm, (f) $z = 25$ mm, (g) $z = 35$ mm, and (h) $z = 45$ mm. The images are normalized by the maximum OH density of their respective plane. Note that for $x < 0$, before the atomizer, the OH remnants from the first stage flame are observed.

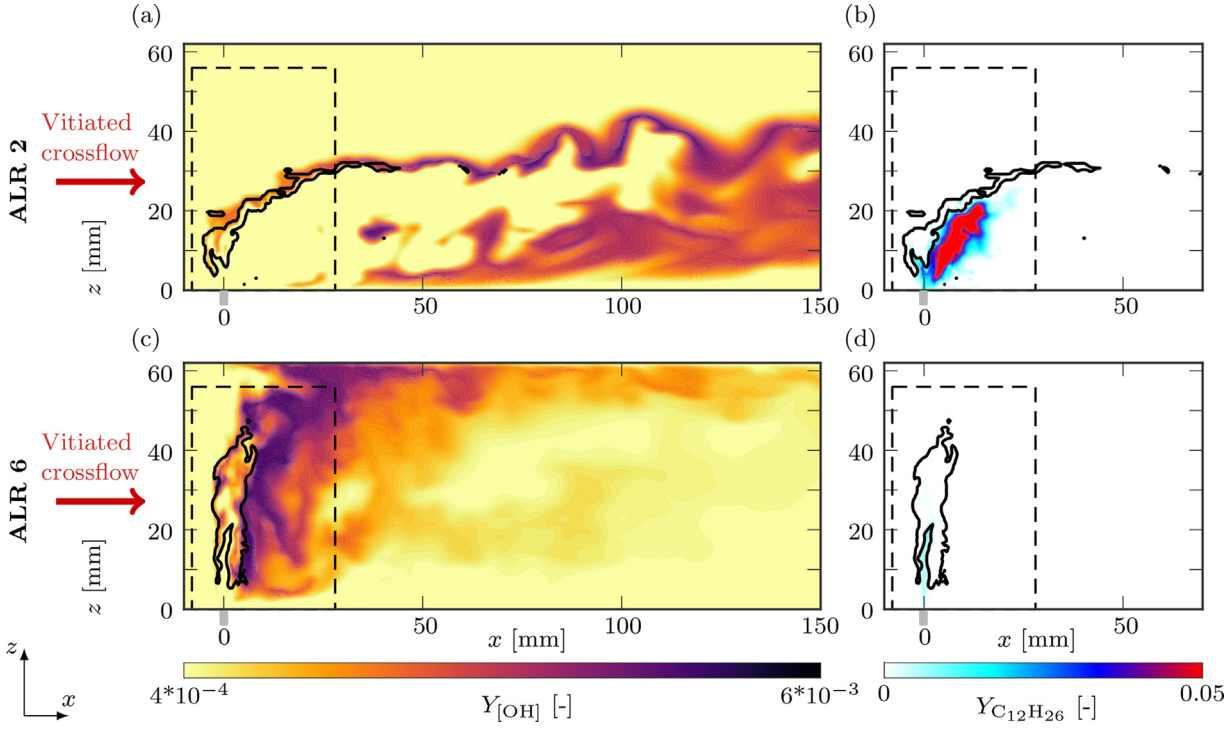

Fig. 8. Instantaneous (a) OH and (b) fuel mass fraction from the LES simulation on the central $x-z$ plane ($y = 0$ mm) of the atomizer at OC3 (5 kW of thermal power and ALR 2). Instantaneous (c) OH and (d) fuel concentration map on the same plane at OC4 (5 kW of thermal power and ALR 6). The black isocontours report 10% of the maximum heat release rate in the domain at the operating condition. The dashed rectangle highlights the experimental Region of Interest (ROI) for PLIF measurements.

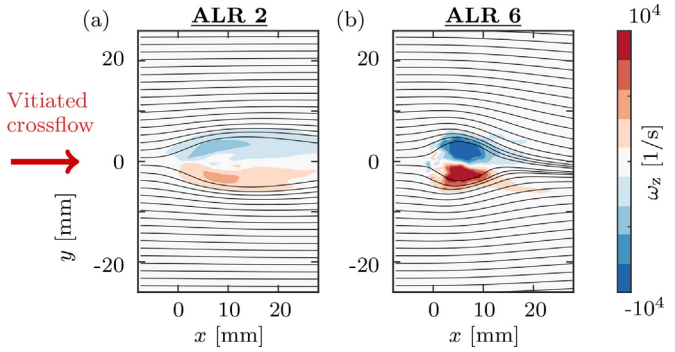

Fig. 9. Time-averaged z vorticity field obtained from LES at (a) OC3 (5 kW of thermal power and ALR 2) at $z = 15$ mm from the injection point and (b) at OC4 (5 kW of thermal power and ALR 6) at $z = 25$ mm. The black lines report the $x - y$ streamlines on the respective planes.

following the reaction region along the upper stretch of the jet. The poor mixing between the fuel and oxidizer results in a high dodecane mass fraction on the leeward side of the jet (b).

The reaction region at ALR 6 is formed along the jet trajectory, resulting in high OH concentration on the leeward side (Fig. 8(c)). The absence of fuel-rich clusters (Fig. 8(d)) confirms the formation of a combustible mixture in the non-reactive jet, induced by the efficient entrainment-induced mixing with the crossflow.

The atomization air velocity influences the penetration of a transverse kerosene spray in a crossflow, as described by the two-phase momentum ratio J given in Eq. (1) from [38]. Previous studies [27,63] have shown that higher jet penetration results in a stronger entrainment-induced mixing between the two streams. Therefore, in the current configuration, the ALR variation is linked to the formation of the reaction regions as it controls the mixing between the fuel spray and the oxidizer-rich crossflow.

Figure 9 reports the out-of-plane z vorticity field, superimposed to the $x - y$ velocity streamlines at ALR 2 at $z = 15$ mm (a) and ALR 6 at $z = 25$ mm (b). The vortical structures are analyzed at the z location of the centroid of the OH* chemiluminescence signal identified in Section 4.1, employed to identify the different penetration of the reaction region induced by the ALR variation. The vorticity maps refer to the experimental Region of Interest (ROI), as simulations confirmed that the largest share of HRR is concentrated in this area.

At ALR 2 (Fig. 9(a)), a weak vortical region is formed on the windward side of the jet due to its small penetration resulting in poor entrainment-induced mixing between the two streams. On the other hand, at ALR 6 (Fig. 9(b), the high magnitudes of the z vorticity highlight the presence of significant entrainment of the crossflow by the jet, which aids efficient mixing between the fuel and the oxidizer streams.

The comparison of the average z vorticity at different ALRs has highlighted pronounced differences in the average vorticity field induced by the jet penetration variation. The change of flow field structures significantly influences the mixing characteristics. The analysis of individual vortices is used to quantify the extent and location of turbulent mixing between the two conditions. Regions of strong rotation in the flow field are identified using the swirling strength (λ), defined as the complex eigenvalue of the velocity gradient tensor $\nabla \vec{v}$. This criterion, introduced by Zhou et al. [64], is not biased by flow dilatation, therefore, applicable to reactive flow fields, as reported by Kolár et al. [65]. Vortices are commonly detected as regions where $\lambda < \varepsilon$, a threshold value accounting for the turbulent nature of the flow field. Since identifying a global threshold value inextricably associates the extension and strength of the vortices, Bremer et al. [66] proposed the application of topological segmentation to find local thresholds. Vortices are identified utilizing relevance, a metric that computes local threshold values as the relative difference in swirling strength with respect to a local maximum. This variable provides a measure of the local strength of a vortex compared to its surrounding, being 1 at the local maximum and 0 at the global minimum in the domain. The application of this method reduces the presence of small noise-induced structures as the identified vortices can be further filtered based on their strength magnitude. Nair et al. [67] employed this approach to describe the shear layer vortices characteristics in a reactive jet in crossflow configuration.

Figure 10 shows the result of the application of the vortex identification algorithm to the $x - z$ midplane $y = 0$ at ALR 2 (a) and 6 (b) superimposed on the normalized out-of-plane vorticity ω_y. The black isocontours correspond to 25% of the maximum relevance. They are overlayed to the y vorticity field, normalized by the atomizer diameter d_{atom} and the air blast jet velocity $\overline{U}_{\text{jet}}$. The black dashed line represents the $x - z$ velocity streamline starting from the atomizer position [0,0]. The location of a vortex in the $x - z$ plane is identified by its coordinates $(x_{\text{vor}}, z_{\text{vor}})$. It is classified as a windward vortex if $x_{\text{vor}} < x_{\text{strmln}}(z = z_{\text{strmln}})$. Vice versa, it is a leeward vortex. Quantitative information on the mixing characteristics is computed using the vortex circulation Γ, calculated in a discrete form on the $x - z$ plane as:

$$\Gamma = \sum_{i \in \text{Vortex}} \omega_{yi}\, \delta A_i, \tag{2}$$

where i refers to a pixel belonging to an identified vortex, ω_{yi} is the y vorticity and δA_i the pixel area.

Vortex structures are identified on the $x - z$ plane for $y = 0$ from 10 simulation snapshots, sampled at a time interval of 30 µs at ALR 2 and 10 µs at ALR 6. The identified vortices are binned in 5 mm wide bins as a function of their distance on the z direction from the injection point Δz_{atom}, between 0 and 60 mm. Figure 10 reports the total circulation (Γ_{tot}) on each bin, i.e., the sum of the circulation of all the vortices on the windward (c) and leeward (d) side. The reported value is normalized by d_{atom} and $\overline{U}_{\text{jet}}$.

Two main differences in terms of the number and distribution of the vortices become apparent from the comparison of (a) and (b) of Fig. 10. At ALR 2, vortical structures are mostly identified on the windward side of the jet, corresponding to the shear mixing structure identified by the y vorticity field. In contrast, a significantly larger number of vortices is formed at ALR 6, approximately equally distributed between the leeward and windward sides.

The ALR variation results in substantially different mixing characteristics, described by the vortex circulation distribution between the leeward and windward sides of the jet, which are visualized in Fig. 10(c) and (d). At ALR 2, relatively high circulation is reported on the windward side of the jet in the vicinity of the injection point ($\Delta z_{\text{atom}} < 20$ mm), rapidly decaying along the z direction. The lower cumulative circulation on the leeward side results from the weak crossflow entrainment. These results confirm that the windward shear layer is the dominant mixing mechanism between the two streams at this condition. At ALR 6, the magnitude of the total circulation is comparable along the z direction and on both sides of the jet. Furthermore, the windward shear layer results in the formation of vortices on low Δz_{atom} planes. However, the higher jet penetration favors a homogeneous distribution of the vortical structures on the windward and leeward sides along the injection direction. Consequently, the efficient mixing between the two streams results in a flame relocation along the jet trajectory, as shown by the HRR isocontour in Fig. 8(c) and (d).

The investigation of the vorticity fields and the vortex circulation distribution at the two ALR conditions has provided insights into the dominant mixing locations and mechanisms. However, the

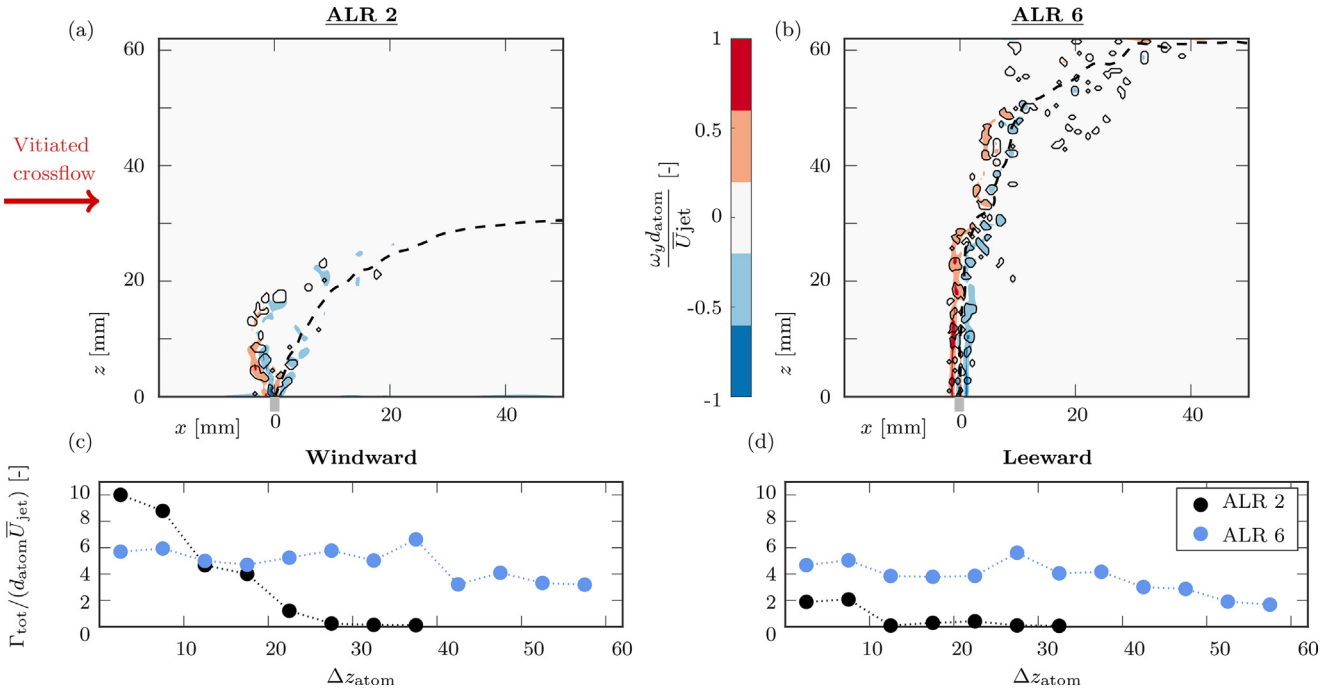

Fig. 10. Instantaneous y vorticity field at ALR 2 (a) OC3 (5 kW of thermal power and ALR 2) and (b) OC4 (5 kW of thermal power and ALR 6). The black isocontours highlight the vortices detected with the identification routine based on swirling strength and local segmentation. The black dashed line shows the $x-z$ velocity streamlines starting from the injection point [0,0] employed to distinguish between leeward and windward vortices. The total circulation on the windward and leeward side of the jet binned at different positions above the injection (Δz_{atom}) point is reported in (c) and (d), respectively. The vorticity and circulations are normalized by the atomizer diameter (d_{atom}) and the airblast jet mean velocity ($\overline{U}_{jet}$).

complexity of the turbulent multiphase spray in crossflow configuration requires an understanding of the behavior of the droplets to provide conclusive insight into the fuel distribution in the domain observed in Fig. 8.

5.2. Droplet distribution

The kerosene spray characteristics are inextricably linked to the ALR variation of the atomizer. In the current section, the spray is investigated by means of the droplet velocity and an analysis of the different timescales governing the system.

The droplets are sampled using the same simulation snapshots described in the previous section. Figure 11 shows the spatial distribution of the droplets on the $x-z$ midplane ($y = \pm 5$ µm) at ALR 2 (a-b) and 6 (c-d). The colormaps report the droplets' x velocity normalized by the bulk crossflow velocity $\overline{U}_{cf}$ (a–c) and the z velocity by the atomization air injection velocities at different ALR conditions (b–d).

The visualization of the droplets on the midplane displays substantial differences in spray dispersion between the two operating conditions. At ALR 2 (Fig. 11(a) and (b)), the midplane droplets distribution exhibits a relatively large spray angle, a small penetration in the crossflow, and the presence of isolated droplets detached from the jet trajectory. The strong spray penetration at ALR 6 (c and d) is associated with a narrow distribution around the jet streamline. The balance between x and z velocity is an indication of the effect of the jet and the crossflow drag on the droplets. Close to the injection point, the high-momentum atomization air jet is responsible for the vertical acceleration of the droplets. Farther away, they are gradually subject to the crossflow drag, which results in an increase of U_x and a simultaneous decrease of U_z. The results of Fig. 11 shows different spray dispersion characteristics as a result of the velocity contributions between the two conditions.

At ALR 2, droplets are monotonically accelerated in the x direction from their injection point, reaching the crossflow velocity ($\overline{U}_{cf} = 35$ m/s) close to their maximum vertical penetration at $z \sim 25$ mm (a). Due to their large inertia at injection, they are accelerated vertically up to only 20% of the kerosene velocity $\overline{U_{jet}}$. Their limited tendency to follow the jet trajectory results in a large spray angle and scattered localized fuel clusters as apparent in the fuel PLIF results in Fig. 5.

The horizontal droplet velocity U_x distribution at ALR 6 shows a monotonic acceleration, similar to lower ALR (Fig. 11(c)). However, while U_x and U_z have similar magnitude at ALR 2, there is a clear predominance of the z velocity component at higher ALR, resulting in a larger maximum vertical penetration ($z \sim 40$ mm). The smaller droplets are rapidly accelerated and have a higher tendency to follow the air-blast airflow due to their smaller inertia (see Fig. 11(d)).

To further analyze the dominant mixing mechanisms related to the droplet size, the global spray evaporation timescales of OCs 3 and 4 are compared to the respective crossflow convective timescales and the penetration timescales. The global spray evaporation timescale is computed according to the d-squared law considering the spray SMD values at the two different ALR conditions:

$$t_{evap} = \frac{d_{SMD}^2}{K} \tag{3}$$

In Eq. (3) K is the mass burning rate of a droplet in a convective environment [68]:

$$K = \frac{4 k_g \mathrm{Nu} \ln(1+B)}{\rho_l c_{pg}}, \tag{4}$$

where k_g is the mean thermal conductivity, B the Spalding mass transfer number, ρ_l the kerosene density and c_{pg} the specific heat capacity. The Nusselt number is calculated as in Turns et al. [68]:

$$\mathrm{Nu} = 2 + \frac{0.555\ \mathrm{Re}^{1/2}\ \mathrm{Pr}^{1/3}}{[1 + 1.232/(\mathrm{Re}\ \mathrm{Pr}^{4/3})]^{1/2}}, \tag{5}$$

Re is the Reynolds number of the droplets, and Pr is the Prandtl number. The values are calculated at $\overline{T}$, defined as the average of

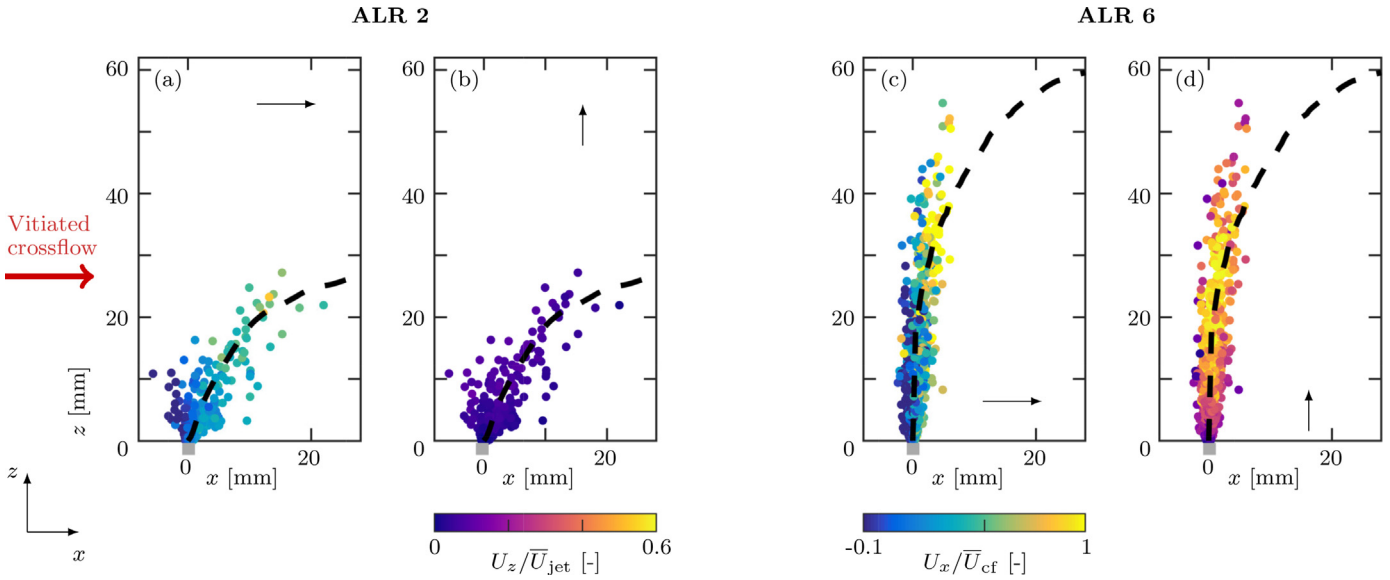

Fig. 11. Scatter plot of the droplet location at the central $y = 0 \pm 5$ μm $x - z$ plane. (a) The normalized x velocity of droplets for OC3 (5 kW of thermal power and ALR 2), (b) the normalized z velocity of droplets for OC3, (c) the normalized x velocity of droplets for OC4 (5 kW of thermal power and ALR 6), and (d) the normalized z velocity of droplets for OC4. The droplets' x velocity is normalized by the average crossflow velocity $\overline{U}_{cf}$ (35 m/s), and the z velocity is normalized by the atomization air injection velocity $\overline{U}_{jet}$ (115 m/s and 345 m/s at ALR 2 and 6, respectively). The dashed lines are the average $x - z$ velocity streamline starting from the injection point [0,0].

the kerosene boiling point T_{boil} and the mean crossflow temperature T_{cf}: $(T_{boil} + T_{cf})/2$. The larger SMD at ALR 2 results in a longer evaporation timescale than ALR 6.

The crossflow convective timescale is computed as:

$$t_{conv} = \frac{l_x}{\overline{U_{cf}}}, \tag{6}$$

where $l_x = 25$ mm is the axial length of the experimental ROI after the atomizer and $U_{cf} = 35$ m/s is the average crossflow velocity.

Finally, the z penetration timescale is computed as:

$$t_z = \frac{l_z}{\overline{U_z}}, \tag{7}$$

where $l_z = 62$ mm is the cross-sectional length of the module and $\overline{U_z}$ the average droplet vertical velocity computed from the distribution of Fig. 11.

The ratio between evaporation and convective timescale (t_{evap}/t_{conv}) provides insights into the effect of the crossflow on the spray distribution in the domain. At ALR 2, this value is larger than 1, underlining that the spray is transported over a distance longer than the experimental ROI before complete evaporation. The ratio (t_{evap}/t_{conv}) becomes < 1 at ALR 6, denoting that in this condition, the spray is fully evaporated within the horizontal extension of the experimental ROI. The spray transport in the x direction, prior to its evaporation, is a significant factor at low ALR due to the longer evaporation timescale.

The situation is reverted in the z direction, where $(t_{evap}/t_z)_{ALR2} < (t_{evap}/t_z)_{ALR6}$. At ALR 2, the large inertia of the droplets results in an overall lower vertical acceleration and penetration (Fig. 11). On the contrary, the smaller droplets at ALR 6 are more subject to the drag induced by the high-velocity jet, resulting in a higher overall U_z. Therefore, droplets tend to penetrate vertically in the crossflow, following the air jet, as visualized in Fig. 11(d).

The timescale analysis reveals a different interplay between evaporation and either crossflow convection or vertical penetration of the droplets. The larger SMD at ALR 2 results in a comparably slower evaporation timescale and a larger own inertia compared to higher ALR. In this case, the crossflow drag has a larger impact on the spray distribution than the vertical transport, resulting in the fuel clustering on the leeward side, observed in Fig. 8(b). The reaction region is therefore localized on the windward side shear layer, where the fuel-rich leeward area and the oxidizer-rich crossflow mix, as highlighted by the vortex identification of Fig. 10.

The combination of the higher momentum atomization air jet and smaller droplet size distribution at ALR 6 results in the opposite trend. The shorter droplet evaporation time reduces the effect of the crossflow drag on the spray compared to the one of the high-velocity vertical jet. At the same time, the strong jet penetration favors an efficient entrainment-induced mixing with the crossflow on the leeward side, resulting in the formation of a homogeneous mixture prior to the reaction (Fig. 8(d)).

6. Conclusions

This study presents an experimental and numerical investigation of a reactive spray in vitiated crossflow configuration. The change in reaction front location and morphology induced by the variation of the air-to-liquid mass flow ratio (ALR) is tracked down to the interplay between the mixing and spray characteristics.

A low ALR is associated with a low J, related to a small air jet penetration and a weak entrainment-induced mixing between the two streams. The droplets timescale analysis highlights the predominance of crossflow convection over vertical penetration within their evaporation time, favoring fuel clustering on the leeward side of the jet. The shear layer between the two perpendicular streams results in comparatively high vorticity on the windward side of the jet in the vicinity of the injection point. The main reaction is therefore concentrated in a thick layer on the windward side of the jet, where shear induces an inefficient mixing between the fuel-rich jet and the oxidizer-rich crossflow. At the same time, the larger spray SMD results in individual droplets or droplet clusters penetrating the vitiated crossflow, where they evaporate and burn locally.

On the other hand, high ALR is associated with comparably high jet penetration and small spray SMD. The high penetration induces strong entrainment of the vitiated crossflow. The smaller droplets have a higher tendency to follow the transverse atomization air jet while evaporating and mixing with the crossflow, resulting in the absence of fuel clusters. The reaction forms a distributed high-OH-intensity area on the leeward side of the jet, composed of individ-

ual sharp gradients related in literature to the formation of thin reaction regions in the gaseous MILD combustion regime. The results of this paper provide insights into the behavior of air-assisted sprays in the vitiated environment. These constitute a stepping stone for developing low-emissions liquid fuel combustion regimes for gas turbine applications.

Declaration of Competing Interest

The authors declare that they have no known competing financial interests or personal relationships that could have appeared to influence the work reported in this paper.

Acknowledgments

This project has received funding from the Clean Sky 2 Joint Undertaking (JU) under grant agreement LEAFINNOX No 831804 and the European Research Council under the ERC Consolidator Grant (No. 820091) TORCH (2019–2024). Clean Sky 2 Joint Undertaking (JU) receives support from the European Union's Horizon 2020 research and innovation programme and the Clean Sky 2 JU members other than the Union. The content of this article reflects only the authors' view. The Clean Sky 2 Joint Undertaking is not responsible for any use that may be made of the information it contains.

References

[1] European Aviation Safety Agency, European Environment Agency and EUROCONTROL, European aviation environmental report, 2022.
[2] Y. Liu, X. Sun, V. Sethi, D. Nalianda, Y.G. Li, L. Wang, Review of modern low emissions combustion technologies for aero gas turbine engines, Prog. Aerosp. Sci. 94 (2017) 12–45.
[3] A.A. Perpignan, A. Gangoli Rao, D.J. Roekaerts, Flameless combustion and its potential towards gas turbines, Prog. Energy Combust. Sci. 69 (2018) 28–62, doi:10.1016/j.pecs.2018.06.002.
[4] S. Kruse, B. Kerschgens, L. Berger, E. Varea, H. Pitsch, Experimental and numerical study of MILD combustion for gas turbine applications, Appl. Energy 148 (2015) 456–465, doi:10.1016/j.apenergy.2015.03.054.
[5] A.E. Khalil, A.K. Gupta, Clean combustion in gas turbine engines using butyl nonanoate biofuel, Fuel 116 (2014) 522–528, doi:10.1016/j.fuel.2013.08.022.
[6] R. Weber, J.P. Smart, W.V. Kamp, On the (MILD) combustion of gaseous, liquid, and solid fuels in high temperature preheated air, Proc. Combust. Inst. 30 II (2) (2005) 2623–2629, doi:10.1016/j.proci.2004.08.101.
[7] M. Noor, A.P. Wandel, T. Yusaf, Mild combustion: the future for lean and clean combustion technology, Int. Rev. Mech. Eng. 8 (1) (2014) 251–257.
[8] J.A. Wünning, J.G. Wünning, Flameless oxidation to reduce thermal no-formation, Prog. Energy Combust. Sci. 23 (1) (1997) 81–94, doi:10.1016/s0360-1285(97)00006-3.
[9] A. Cavaliere, M. De Joannon, Mild combustion, Prog. Energy Combust. Sci. 30 (4) (2004) 329–366, doi:10.1016/j.pecs.2004.02.003.
[10] C. Galletti, A. Parente, L. Tognotti, Numerical and experimental investigation of a mild combustion burner, Combust. Flame 151 (2007) 649–664, doi:10.1016/j.combustflame.2007.07.016.
[11] G. Sorrentino, P. Sabia, M.D. Joannon, A. Cavaliere, R. Ragucci, The effect of diluent on the sustainability of mild combustion in a cyclonic burner, Flow, Turbul. Combust. 96 (2016) 449–468, doi:10.1007/s10494-015-9668-3.
[12] G.G. Szegö, B.B. Dally, G.J. Nathan, Scaling of NOx emissions from a laboratory-scale mild combustion furnace, Combust. Flame 154 (2008) 281–295, doi:10.1016/j.combustflame.2008.02.001. 170 citations
[13] S. Iavarone, A. Parente, NOx formation in mild combustion: potential and limitations of existing approaches in CFD, Front. Mech. Eng. 6 (2020), doi:10.3389/fmech.2020.00013.
[14] Y. Minamoto, N.A.K. Doan, N. Swaminathan, Mild combustion, Advanced Turbulent Combustion Physics and Applications, Cambridge University Press (2021), pp. 240–280, doi:10.1017/9781108671422.007.
[15] I.E. Helou, J. Foale, A. Giusti, J.A. Sidey, E. Mastorakos, Experimental and numerical investigation of an ultra-low NOx methane reactor, Energy Procedia 120 (2017) 214–221, doi:10.1016/j.egypro.2017.07.167. Description of the LEAF burner. The combustor operates in non premixed combustion with preheating of both
[16] P.M.D. Oliveira, D. Fredrich, G.D. Falco, I.E. Helou, A. D'Anna, A. Giusti, E. Mastorakos, Soot-free low-NOx aeronautical combustor concept: the lean azimuthal flame for kerosene sprays, Energy Fuels 35 (2021) 7092–7106, doi:10.1021/acs.energyfuels.0c03860.
[17] L. Miniero, K. Pandey, G.D. Falco, A. D'Anna, N. Noiray, Soot-free and low-no combustion of Jet A-1 in a lean azimuthal flame (LEAF) combustor with hydrogen injection, Proc. Combust. Inst. (2022), doi:10.1016/j.proci.2022.08.006.
[18] K. Pandey, L. Miniero, U. Doll, P.M. de Oliveira, E. Mastorakos, N. Noiray, Topological transitions of Jet A-1 lean azimuthal flames (leaf), Proc. Combust. Inst. (2022), doi:10.1016/j.proci.2022.08.034.
[19] N. Yilmaz, A. Atmanli, Sustainable alternative fuels in aviation, Energy 140 (2017) 1378–1386, doi:10.1016/j.energy.2017.07.077.
[20] F. Wang, P. Li, G. Wang, J. Mi, Moderate and intense low-oxygen dilution (mild) combustion of liquid fuels: a review, Energy Fuels 36 (2022) 8026–8053, doi:10.1021/acs.energyfuels.2c01383.
[21] F. Xing, A. Kumar, Y. Huang, S. Chan, C. Ruan, S. Gu, X. Fan, Flameless combustion with liquid fuel: a review focusing on fundamentals and gas turbine application, Appl. Energy 193 (2017) 28–51, doi:10.1016/j.apenergy.2017.02.010.
[22] A. Williams, D. Shcherbik, O. Bibik, E. Lubarsky, B.T. Zinn, Autoignition of a Jet-A fuel spray in a high temperature vitiated air flow, Proc. ASME Turbo Expo 4A (2015), doi:10.1115/GT2015-42199.
[23] H.C. Rodrigues, M.J. Tummers, E.H. van Veen, D.J. Roekaerts, Spray flame structure in conventional and hot-diluted combustion regime, Combust. Flame 162 (2015) 759–773, doi:10.1016/j.combustflame.2014.07.033.
[24] L. Ma, D. Roekaerts, Numerical study of the multi-flame structure in spray combustion, Proc. Combust. Inst. 36 (2) (2017) 2603–2613.
[25] S. Gallot-Lavallée, W. Jones, A. Marquis, Large eddy simulation of an ethanol spray flame with secondary droplet breakup, Flow, Turbul. Combust. 107 (3) (2021) 709–743.
[26] A.R. Karagozian, The jet in crossflow, Phys. Fluids 26 (2014) 101303, doi:10.1063/1.4895900.
[27] L. Cortelezzi, A.R. Karagozian, On the formation of the counter-rotating vortex pair in transverse jets, J. Fluid Mech. 446 (2001) 347–373, doi:10.1017/s0022112001005894.
[28] O. Schulz, N. Noiray, Autoignition flame dynamics in sequential combustors, Combust. Flame 192 (2018) 86–100, doi:10.1016/j.combustflame.2018.01.046.
[29] R. Solana-Pérez, L. Miniero, S. Shcherbanev, M. Bothien, N. Noiray, Morphology and dynamics of a premixed hydrogen-methane-air jet flame in hot vitiated turbulent crossflow, Proc. ASME Turbo Expo 4B-2020 (2020), doi:10.1115/GT2020-16282.
[30] J.A. Wagner, S.W. Grib, M.W. Renfro, B.M. Cetegen, Flowfield measurements and flame stabilization of a premixed reacting jet in vitiated crossflow, Combust. Flame 162 (2015) 3711–3727, doi:10.1016/j.combustflame.2015.07.010.
[31] P.P. Panda, O. Busari, M. Roa, R.P. Lucht, Flame stabilization mechanism in reacting jets in swirling vitiated crossflow, Combust. Flame 207 (2019) 302–313, doi:10.1016/j.combustflame.2019.06.005.
[32] R. Sullivan, B. Wilde, D.R. Noble, J.M. Seitzman, T.C. Lieuwen, Time-averaged characteristics of a reacting fuel jet in vitiated cross-flow, Combust. Flame 161 (2014) 1792–1803, doi:10.1016/j.combustflame.2013.12.022.
[33] T. Yi, B.R. Halls, N. Jiang, J. Felver, M. Sirignano, B.L. Emerson, T.C. Lieuwen, J.R. Gord, S. Roy, Autoignition-controlled flame initiation and flame stabilization in a reacting jet in crossflow, Proc. Combust. Inst. 37 (2019) 2109–2116, doi:10.1016/j.proci.2018.06.057.
[34] J. Sidey, E. Mastorakos, Visualization of mild combustion from jets in cross-flow, Proc. Combust. Inst. 35 (2015) 3537–3545, doi:10.1016/j.proci.2014.07.028.
[35] O. Schulz, E. Piccoli, A. Felden, G. Staffelbach, N. Noiray, Autoignition-cascade in the windward mixing layer of a premixed jet in hot vitiated crossflow, Combust. Flame 201 (2019) 215–233, doi:10.1016/j.combustflame.2018.11.012. https://linkinghub.elsevier.com/retrieve/pii/S0010218018304875
[36] R. Solana-Pérez, O. Schulz, N. Noiray, Simulation of the self-ignition of a cold premixed ethylene-air jet in hot vitiated crossflow, Flow, Turbul. Combust. 106 (4) (2021) 1295–1311.
[37] A.H. Lefebvre, V.G. McDonell, Atomization and Sprays, CRC Press, 2017, doi:10.1201/9781315120911.
[38] M.Y. Leong, V.G. McDonell, G.S. Samuelsen, Effect of ambient pressure on an airblast spray injected into a crossflow, J. Propul. Power 17 (2001) 1076–1084, doi:10.2514/2.5846.
[39] A. Sinha, R.S. Prakash, A.M. Mohan, R.V. Ravikrishna, Airblast spray in crossflow - structure, trajectory and droplet sizing, Int. J. Multiph. Flow 72 (2015) 97–111, doi:10.1016/j.ijmultiphaseflow.2015.02.008.
[40] D. Fredrich, L. Miniero, K. Pandey, W.P. Jones, N. Noiray, A. Giusti, Large eddy simulation of a reacting kerosene spray in hot vitiated cross-flow, Flow, Turbul. Combust. (2022), doi:10.1007/s10494-022-00355-5.
[41] C.T. Chong, S. Hochgreb, Effect of atomizing air flow on spray atomization of an internal-mix twin-fluid atomizer, At. Sprays 25 (2015) 657–673, doi:10.1615/AtomizSpr.2015011361.
[42] D.G. Goodwin, Cantera: an open-source, object-oriented software suite for combustion, 2006.

[43] M. Kumar, S. Karmakar, S. Kumar, S. Basu, Experimental investigation on spray characteristics of Jet A-1 and alternative aviation fuels, Int. J. Spray Combust. Dyn. 13 (2021) 54–71.
[44] N.K. Rizk, A.H. Lefebvre, Spray characteristics of plain-jet airblast atomizers, J. Eng. Gas Turbine Power 106 (1984) 634–638, doi:10.1115/83-gt-138.
[45] M. Orain, P. Baranger, C. Ledier, J. Apeloig, F. Grisch, Fluorescence spectroscopy of kerosene vapour at high temperatures and pressures: potential for gas turbines measurements, Appl. Phys. B 116 (2014) 729–745, doi:10.1007/s00340-013-5756-z.
[46] A. Arnold, R. Bombach, B. Käppeli, A. Schlegel, Quantitative measurements of oh concentration fields by two-dimensional laser-induced fluorescence, Appl. Phys. B 64 (5) (1997).
[47] J. Heinze, U. Meier, T. Behrendt, C. Willert, K.P. Geigle, O. Lammel, R. Lückerath, PLIF thermometry based on measurements of absolute concentrations of the oh radical, Z. Phys. Chem. 225 (2011) 1315–1341, doi:10.1524/zpch.2011.0168.
[48] W. Demtröder, Laser Spectroscopy 2, vol. 5, Springer, 2014.
[49] M. Weilenmann, U. Doll, R. Bombach, A. Blondé, D. Ebi, Y. Xiong, N. Noiray, Linear and nonlinear entropy-wave response of technically-premixed jet-flames-array and swirled flame to acoustic forcing, Proc. Combust. Inst. 000 (2020) 1–9, doi:10.1016/j.proci.2020.06.233.
[50] U. Doll, G. Stockhausen, J. Heinze, U. Meier, C. Hassa, I. Bagchi, Temperature measurements at the outlet of a lean burn single-sector combustor by laser optical methods, J. Eng Gas Turbine Power 139 (2017), doi:10.1115/1.4034355.
[51] D. Fredrich, W.P. Jones, A.J. Marquis, The stochastic fields method applied to a partially premixed swirl flame with wall heat transfer, Combust. Flame 205 (2019) 446–456, doi:10.1016/j.combustflame.2019.04.012.
[52] M. Nehse, J. Warnatz, C. Chevalier, Kinetic modeling of the oxidation of large aliphatic hydrocarbons, Symp. (Int.) Combust. 26 (1) (1996) 773–780, doi:10.1016/S0082-0784(96)80286-4.
[53] R.S. Miller, K. Harstad, J. Bellan, Evaluation of equilibrium and non-equilibrium evaporation models for many-droplet gas-liquid flow simulations, Int. J. Multiph. Flow 24 (1998) 1025–1055, doi:10.1016/S0301-9322(98)00028-7.
[54] M. Bini, W.P. Jones, Large-eddy simulation of particle-laden turbulent flows, J. Fluid Mech. 614 (2008) 207–252, doi:10.1017/S0022112008003443.
[55] B. Higgins, M.Q. McQuay, F. Lacas, J.C. Rolon, N. Darabiha, S. Candel, Systematic measurements of oh chemiluminescence for fuel-lean, high-pressure, premixed, laminar flames, Fuel 80 (2001) 67–74, doi:10.1016/S0016-2361(00)00069-7.
[56] H.N. Najm, P.H. Paul, C.J. Mueller, P.S. Wyckoff, On the adequacy of certain experimental observables as measurements of flame burning rate, Combust. Flame 113 (3) (1998) 312–332.
[57] B.O. Ayoola, R. Balachandran, J.H. Frank, E. Mastorakos, C.F. Kaminski, Spatially resolved heat release rate measurements in turbulent premixed flames, Combust. Flame 144 (2006) 1–16, doi:10.1016/j.combustflame.2005.06.005.
[58] J.O. Keller, K. Saito, Measurements of the combusting flow in a pulse combustor, Combust. Sci. Technol. 53 (1987) 137–163, doi:10.1080/00102208708947024.
[59] R. Santhosh, S. Basu, Transitions and blowoff of unconfined non-premixed swirling flame, Combust. Flame 164 (2016) 35–52, doi:10.1016/j.combustflame.2015.10.034.
[60] J. Renner, M. March, C. Hirsch, T. Sattelmayer, Flame dynamics in the lean burnout zone of an RQLcombustion chamber - response to primary zone velocity fluctuations, Int. J. Spray Combust. Dynam. 14 (2022) 238–250, doi:10.1177/17568277221128169.
[61] A.R. Karagozian, Transverse jets and their control, Prog. Energy Combust. Sci. 36 (2010) 531–553, doi:10.1016/j.pecs.2010.01.001.
[62] Y. Minamoto, N. Swaminathan, Scalar gradient behaviour in mild combustion, Combust. Flame 161 (2014) 1063–1075, doi:10.1016/j.combustflame.2013.10.005.
[63] Y. Kamotani, I. Greber, Experiments on a turbulent jet in a cross flow, AIAA J. 10 (1972) 1425–1429, doi:10.2514/3.50386.
[64] J. Zhou, R.J. Adrian, S. Balachandar, T.M. Kendall, Mechanisms for generating coherent packets of hairpin vortices in channel flow, J. Fluid Mech. 387 (1999) 353–396, doi:10.1017/S002211209900467X.
[65] V. Kolàř, Compressibility effect in vortex identification, AIAA J. 47 (2009) 473–475, doi:10.2514/1.40131.
[66] P.T. Bremer, A. Gruber, J.C. Bennett, A. Gyulassy, H. Kolla, J.H. Chen, R.W. Grout, Identifying turbulent structures through topological segmentation, Commun. Appl. Math. Comput. Sci. 11 (2016) 37–53, doi:10.2140/camcos.2016.11.37.
[67] V. Nair, M. Sirignano, B.L. Emerson, T.C. Lieuwen, Combustion and flame position impacts on shear layer dynamics in a reacting jet in cross-flow, J. Fluid Mech. 942 (2022), doi:10.1017/jfm.2022.387.
[68] S.R. Turns, et al., Introduction to Combustion, vol. 287, McGraw-Hill Companies New York, NY, USA, 1996.